UMYU Scientifica, Vol. 4 NO. 1, March 2025, Pp 168 – 178
https://doi.org/10.56919/usci.2541.017
ISSN: 2955 – 1145 (print); 2955 – 1153 (online)
A periodical of the Faculty of Natural and Applied Sciences, UMYU, Katsina

ORIGINAL RESEARCH ARTICLE

Theoretical Study of the Transport Properties of Cs_2NaBiX_6 $[X = Br, I]$ Double Perovskite and its Stability for Thermoelectric Applications

Tersoo Atsue[1*], and Oluwole E. Oyewande[2]
[1]Theoretical and Computational Physics Unit, Department of Physics, Federal University Dutsin-Ma, Katsina, Nigeria
[2]Theoretical Physics Unit, Department of Physics, Faculty of Science, University of Ibadan, Ibadan, Nigeria

ABSTRACT

Perovskite materials are very useful in photovoltaic applications, and their application can also be extended to thermoelectric devices. Double perovskites have lately attracted interest due to research into their characteristics and prospective applications in thermoelectric devices. Cs_2NaBiX_6 Double Perovskites (DPs) are considered in this study to cross-examine their transport, mechanical, and vibrational properties from an ab-initio method to determine their potential for thermoelectric application. The transport coefficients evaluated in this study include the Seebeck coefficient, electrical conductivity, thermal conductivity, power factor, and the thermoelectric figure of merit. The properties are calculated as a function of chemical potential at a temperature range of 300 K to 800 K. The findings show a high figure of merit of a near unity at all temperature ranges. The mechanical properties suggest that the materials satisfy the Born stability criteria for cubic crystals and are thus stable mechanically. The vibrational properties through phonon dispersion curves suggest the materials lack dynamical stability as a result of imaginary frequencies present at the Brillouin zone boundary and center (Γ) of the DP materials. The materials can, therefore, be useful for thermoelectric applications, allowing for the operation of their devices even at high temperatures.

ARTICLE HISTORY

Received December 20, 2024
Accepted February 22, 2025
Published February 24, 2025

KEYWORDS

stability criteria, electrical conductivity, Double perovskite, imaginary frequency, figure of merit.

INTRODUCTION

Scientific researchers have found attraction in the inorganic perovskites owing to their numerous intriguing physical properties which could lead to the commercialization of devices from their application. Applications of perovskites are not limited to solar cells as they span through several optoelectronic components. Such features of uniqueness in perovskite materials include their tunable bandgaps, high optical absorption, low effective masses, long carrier lifetime, non-high exciton binding energy, and others (Aslam et al., 2021; Filip & Giustino, 2016). Additionally, they are naturally abundant, affordable in cost, and easily processed, which puts them ahead of many other classes of materials (Chen et al., 2014; Kim et al., 2012).

Undoubtedly, the most efficient halide perovskites are those containing lead metal cations. Lead is, however, toxic and limits the commercialization of devices using such materials as they are not environment friendly (Lyu et al., 2017; Pitaro et al., 2022; Slavney et al., 2017). Researchers now have to search for new metal cations that are less or toxic-free as a replacement for lead cations in the perovskite design. Tin (Sn^{2+}) and germanium (Ge^{2+}) (Hao et al., 2014; Krishnamoorthy et al., 2015; Yang et al., 2016) were the first cations used for the replacement of lead in the halide perovskite. The perovskite structure was perfect when lead was replaced by Sn^{2+} and Ge^{2+}, which had the required narrow bandgap but lacked stability since they can oxidize rapidly from the 2+ state to the 4+ state (Leijtens et al., 2017; Moniruddin et al., 2018; Roknuzzaman et al., 2019). Subsequently, researchers have used other elements with a 2+ state, such as magnesium (Filip & Giustino, 2016; Johnson et al., 2019), to replace lead, and favorable results were obtained. The quest for lead-free perovskite also propelled researchers to use double metal cations (monovalent and trivalent cations) as a lead substitute, leading to halide double perovskites (DP), starting with the pioneering works of Volonakis *et al.* and Slavney *et al.* (Slavney et al., 2016; Volonakis et al., 2016), and other subsequent works that followed (Filip et al., 2016; McClure et al., 2016).

Researchers' interest in DPs has grown recently, presumably as a result of their allure. A variety of numerical simulations have been applied in the study of materials properties (Oyewande & Adeoti, 2014;

Correspondence: Tersoo Atsue. Theoretical and Computational Physics Unit, Department of Physics, Faculty of Physical Sciences, Federal University Dutsin-Ma, Katsina, Nigeria. ✉ tatsue@fudutsinma.edu.ng.

How to cite: Atsue, T., & Oyewande, O. E. (2025). Theoretical Study of the Transport Properties of Cs_2NaBiX_6 $[X = Br, I]$ Double Perovskite and its Stability for Thermoelectric Applications. *UMYU Scientifica*, 4(1), 168 – 178. https://doi.org/10.56919/usci.2541.017

Oyewande, 2012, 2013), including mathematical modeling and Monte Carlo simulations (Aisida & Oyewande, 2015; Kolebaje et al., 2020; Yewande et al., 2005). Recently, density functional theory (DFT) has greatly armed scientists with the tool to explore the alluring properties of these materials to the extent of finding novel materials for a variety of applications (Sholl & Steckel, 2009). Shi and Du used the DFT technique to study $\mathrm{Cs_2NaInBr_6}$ DP to explain the self-trapping stabilization of narrow bands (Shi & Du, 2015). Also, Zhao et al. employed the DFT tool to investigate the optoelectronic properties of $\mathrm{Cs_2NaBX_6}$ $(\mathrm{B = Bi, Sb\ and\ X = Cl, Br, and\ I})$ DPs (Zhao et al., 2018). Optoelectronic properties of many perovskites have been investigated recently employing DFT techniques, with some researchers exploring bandgap engineering of the materials (Atsue & Oyewande, 2024; Bairwa et al., 2024; Kattan et al., 2023; Mera et al., 2023). To enhance the photovoltaic performance of DP materials, DFT has been utilized to model the solid solutions of such DPs (Atsue et al., 2021; Ogunniranye et al., 2021). It is observed that DFT has been employed to investigate the thermoelectric properties of DP materials for thermoelectric device applications in recent times (Aslam et al., 2021; Atsue & Oyewande, 2024; Ghrib et al., 2021; Joshi et al., 2020; Noor et al., 2021). Cs_2NaBiX_6 $[X = Br, I]$ DPs were among the solid solutions modeled DPs that were investigated for improving photovoltaic performance (Atsue et al., 2021). The materials were observed to satisfy the criteria for forming stable 3-D perovskites which include the Goldschmidt tolerance factor (t), the octahedral factor (μ), and the new tolerance factor (τ) respectively. The thermodynamic stability of the bromide DP was ascertained. The results revealed enhanced characteristics of the materials for photovoltaic applications. These DP materials are however lacked in literature exploring their potentials for thermoelectric applications.

The present study, therefore, employs the DFT technique to investigate the thermoelectric properties of Cs_2NaBiX_6 $[X = Br, I]$ DPs, as well as their mechanical and vibrational properties for stability and thermoelectric applications.

MATERIALS AND METHODS

The material properties of the Cs_2NaBiX_6 DPs were calculated using the density functional theory (DFT) approach. DFT, as a plane wave pseudopotential method, was implemented in the Quantum ESPRESSO (QE) suite (Giannozzi et al., 2017; Giannozzi et al., 2009) for calculations of the relevant properties of the DPs. The exchange-correlation function utilized for the calculation of all the properties was based on the generalized gradient approximation (GGA) described by Perdew-Burke-Ernzerhof revised for solid (PBEsol) (Perdew et al., 2008). The study employed norm-conserving pseudopotentials (NCPPs) (Hamann et al., 1979) to represent electron-ion interactions. For plane wave expansion, the kinetic energy cutoff of the pseudopotentials was optimized to 70 Ry. The Brillouin zone was integrated over the Monkhorst-Pack (Pack & Monkhorst, 1977) k-point mesh of $6 \times 6 \times 6$. The total energy convergence criterion was set to at least $10^{-9}\ Ry$. These settings were used to optimize the lattice parameters of the DPs investigated. The Broyden-Fletcher-Goldfarb-Shanno (BFGS) algorithm (Broyden, 1970a, 1970b) was used for atomic position optimization with the force and energy convergence criteria of less than $10^{-4}\ Ry/\mathrm{Bohr}$ and $10^{-3}\ Ry$ respectively. For the calculation of the transport properties, a solution of the classical Boltzmann transport equation (BTE) was obtained via the constant relaxation-time approximation and the rigid band approximation. The calculation was implemented in the BoltzTrap code. A denser k-point mesh of $16 \times 16 \times 16$ was applied in QE for the non-self-consistent field calculation for the purpose of obtaining reliable transport properties. The mechanical properties of the DP materials were calculated from their elastic constants using a QE dependent package known as the thermo_pw code which is adjudged as been an efficient tool for elastic constants computations (Dal Corso, 2016). The DP materials are cubic crystals and thus require only three elastic constants, C_{11}, C_{12}, and C_{44} to characterize their crystal elasticity (Chung & Buessem, 1967). The vibrational properties were of the DPs were studied through phonon dispersion calculations to assess their dynamical stability. The density functional perturbation theory (DFPT) approach was implemented in QE for the calculations. In the irreducible Brillouin zone, a $2 \times 2 \times 2$ q-point mesh was used for phonon dynamical matrix calculations. The phonon density of states determined at the atomic level was obtained using the quasi-harmonic approximation (qha) code.

RESULTS AND DISCUSSIONS

Structural Properties

The structure of Cs_2NaBiX_6, [where $X = I, Br$] DP is face center cubic with $Fm\bar{3}m$ as space group adopted in its primitive unit cell form containing ten atoms. An XCrySDen (Kokalj, 1999) visualization of the primitive unit cell is presented in **Figure 1.**

Lattice parameters were optimized by applying the PBEsol potential. The energy-volume data acquired through the energy minimization technique were fitted using the Murnaghan equation of state (Murnaghan, 1924) to produce the equilibrium lattice parameter (a Å). **Figures 2(a)** and **(b)**, respectively, show a plot of the total energy against the lattice parameter for the materials $Cs_2NaBiBr_6$ and Cs_2NaBiI_6. The minimum energy point indicates the equilibrium lattice constant for the material. The plots indicate that Cs_2NaBiI_6 [**Figure 2(b)**] acquired more energy than $Cs_2NaBiBr_6$ [**Figure 2(a)**]. This may be due to the fact that Cs_2NaBiI_6 has a longer lattice constant (12.399 Å) than $Cs_2NaBiBr_6$ (11.419 Å) as computed from this study. The computed lattice constants are in agreement with previous literature reports of 12.199 Å and 11.364 Å (Zhao et al., 2018) for

Cs_2NaBiI_6 and $Cs_2NaBiBr_6$ DP compounds respectively. The difference in the lattice constant follows from the difference in the ionic radii of iodine and bromine which is 2.20 Å and (1.96 Å) respectively.

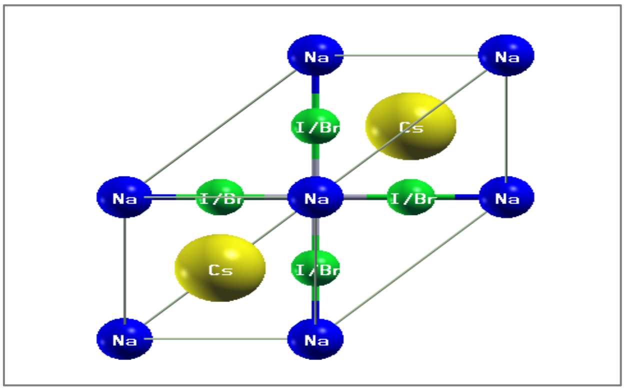

Figure 1: An XCrySDen visualization of the used ten atom primitive unit cell

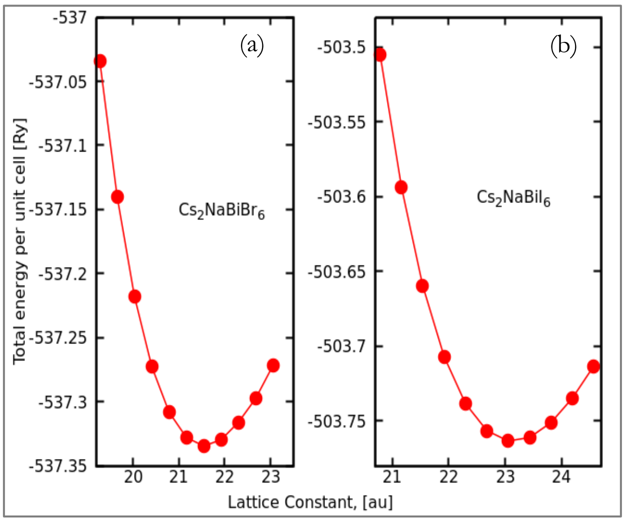

Figure 2: Total energy plot as a function of lattice constant for (a) $Cs_2NaBiBr_6$ and (b) Cs_2NaBiI_6 DP compounds

Thermoelectric properties

A material may be suitable for thermoelectric application, considering the quality of its transport properties. The DP materials considered in this study were used to investigate these properties to understand their full potential in thermoelectric applications. The procedure for calculating the transport coefficients is outlined in the materials and methods section, where the BoltzTrap code was used to implement the classical Boltzmann theory (CBT). The evaluated properties are all dependent on the chemical potential (μ) and temperature (T). Chemical potential (μ), whose value is zero at the Fermi level, is the quantity of energy necessary to subdue coulomb potential and bring electrons into the circuit. For a p-type material, a negative value of μ while a positive value exists for an n-type material (Haq et al., 2021; Noor et al., 2021).

The Seebeck coefficient (S) creates a potential difference between two edges of a material to represent temperature changes between them (Joshi et al., 2020; Noor et al., 2021). It is a crucial transport coefficient calculated using Eq. (1)

$$S_{\alpha\beta}(T;\mu) = \frac{1}{eT\Omega\sigma_{\alpha\beta}(T;\mu)} \int \sigma_{\alpha\beta}(\varepsilon)(\epsilon - \mu)\left\{-\frac{\partial f_\mu(T;\varepsilon)}{\partial\varepsilon}\right\} d\varepsilon \qquad (1)$$

From Eq. (1), α and β denote the transport tensor indices, whereas e is the charge on the electron, Ω is the volume of unit cell, and f denotes the Fermi Dirac distribution function. The results of the Seebeck coefficient for the DPs investigated are displayed graphically in **Figure (3).**

From **Figure 3**, the Seebeck coefficient, S, can be observed to decrease at increasing temperature, T, which is expected for a good thermoelectric material. This decrease can be conspicuously noticed in **Figure 3(c)**, which shows the Seebeck coefficient versus temperature. The trend of the results obtained is similar to those of other DP materials (Aslam et al., 2021; Haq et al., 2021; Joshi et al., 2020) in the literature. In **Figure 3(a)**, the Seebeck coefficient at 300 K has a maximum value of $2.960\ mVK^{-1}$. The value decreased to $1.777\ mVK^{-1}$ at an elevated temperature of 800 K. The Seebeck coefficient generally exhibits two peaks of positive and negative values, which are $2.960\ mVK^{-1}$ and $-2.769\ mVK^{-1}$ at 300 K, $2.389\ mVK^{-1}$ and $-2.381\ mVK^{-1}$ at 600 K, and $1.777\ mVK^{-1}$ and $-1.783\ mVK^{-1}$ at 800 K, respectively. In **Figure 3(b)**, the maximum S value at 300 K is $2.963\ mVK^{-1}$ slightly more than that in **Figure 3(a)**. This implies low carrier mobility at lower temperatures leading to high S values. The carrier mobility increases as the temperature is raised, leading to higher electronic conductivity as S is lowered. At an elevated temperature of 800 K, it decreased to $1.253\ mVK^{-1}$. The positive and negative peak values are $2.963\ mVK^{-1}$ and $-2.738\ mVK^{-1}$ at 300 K, $1.678\ mVK^{-1}$ and $-1.622\ mVK^{-1}$ at 600 K, and $1.253\ mVK^{-1}$ and $-1.212\ mVK^{-1}$ at 800 K respectively. The peak values of S for the DPs investigated occurred within the region of negative chemical potential values, and the positive peaks are higher than the negative peaks, suggesting that p-type doping of the materials may be favorable. Apart from the room temperature where the S value of Cs_2NaBiI_6 DP is slightly higher than that of $Cs_2NaBiBr_6$ DP, at elevated temperatures, S values of $Cs_2NaBiBr_6$ DP are higher than those of Cs_2NaBiI_6 DP probably due to larger bandgap of $Cs_2NaBiBr_6$ DP.

The electrical conductivity (σ) is another useful property of the transport coefficient computed using Eq. (2) given by

$$\sigma_{\alpha\beta}(T;\mu) = \frac{1}{\Omega}\int \sigma_{\alpha\beta}(\varepsilon)\left\{-\frac{\partial f_\mu(T;\varepsilon)}{\partial\varepsilon}\right\} d\varepsilon \qquad (2)$$

where the coefficient of electrical conductivity, $\sigma_{\alpha\beta}(\varepsilon)$ is given by

$$\sigma_{\alpha\beta}(\varepsilon)=\frac{e^2}{N}\sum_{i,k}\tau_i\, k v_\alpha(i,k) v_\beta(i,k)\delta(\varepsilon-\varepsilon_{i,k}) \qquad (3)$$

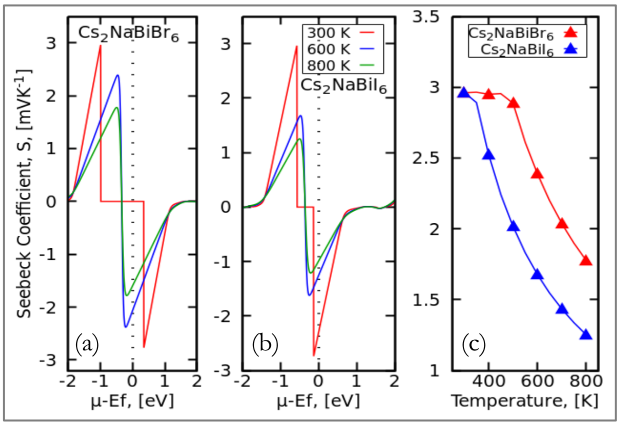

Figure 3: Seebeck coefficient curves as dependent of chemical potential and temperature for (a) $Cs_2NaBiBr_6$, (b) Cs_2NaBiI_6 DPs, and (c) Seebeck coefficient as function of temperature

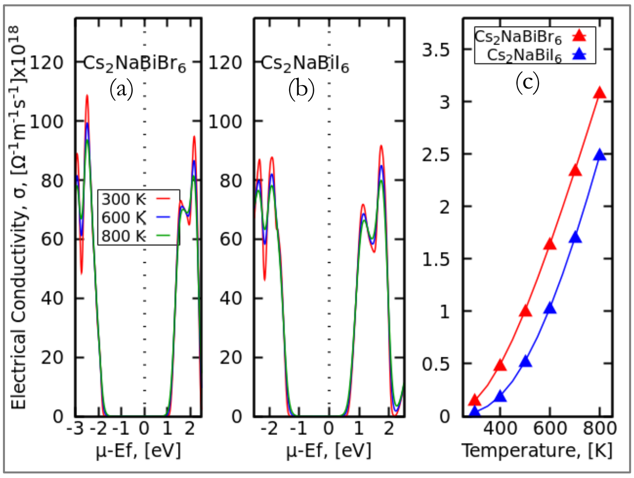

Figure 4: Chemical potential and temperature dependent electrical conductivity curves for (a) $Cs_2NaBiBr_6$, (b) Cs_2NaBiI_6 DPs, and (c) electrical conductivity as a function of temperature

The relaxation time is denoted by τ, the sampled k-points number by N, the band energy is represented by $\varepsilon(k)$, while the band velocity utilizes the symbol $v(k)$.

The electrical conductivity results are shown in **Figure 4**, plotted as a function of chemical potential and temperature. The temperature used ranged from 300 K to 800 K and the results show a remarkable trend agreement with previous results of similar DPs (Joshi et al., 2020). The σ of the DPs exhibit similar results across the chemical potential values at all temperatures. The maximum value of σ for $Cs_2NaBiBr_6$ in **Figure 4(a)** is $110\times10^{18}\ \Omega^{-1}m^{-1}s^{-1}$ at 300 K and $94\times10^{18}\ \Omega^{-1}m^{-1}s^{-1}$ at an elevated temperature of 800K. The peak values at all temperatures are around the chemical potential value of -2.5 eV suggesting more hole carriers are present in the DP material. In **Figure 4(b)** at 300 K, the maximum value of σ for Cs_2NaBiI_6 is $92\times10^{18}\ \Omega^{-1}m^{-1}s^{-1}$ and is lower than that in **Figure 4(a)**. At an elevated temperature of 800 K, the value is found to be $80\times10^{18}\ \Omega^{-1}m^{-1}s^{-1}$. In **Figure 4(c),** the DPs exhibit semiconducting behavior in which free charge carriers gain heat energy, causing them to flow from the hot region of the material to the colder region, thereby enhancing the electrical conductivity (Mahmood et al., 2019).

Phonons (κ_{ph}) and electrons (κ_e) thermal conductivities are responsible for a material's heat flow-related thermal conductivity (Haque & Hossain, 2019; Noor et al., 2021). In this investigation, only the electronic component of thermal conductivity is estimated since phonon contribution is outside the purview of the BoltzTraP code, and its calculation is computationally expensive. The electronic thermal conductivity is computed using Eq. (4), given by

$$\kappa^e_{\alpha\beta}(T;\mu)=\frac{1}{e^2T}\int\sigma_{\alpha\beta}(\varepsilon)(\varepsilon-\mu)^2\left\{-\frac{\partial f_\mu(T;\varepsilon)}{\partial\varepsilon}\right\}d\varepsilon \qquad (4)$$

The results of the electronic thermal conductivity are shown in **Figure 5(a)** for $Cs_2NaBiBr_6$, and **Figure 5(b)** Cs_2NaBiI_6 DPs. The electronic thermal conductivity (κ_e) results are observed to increase at elevated temperatures for all DPs investigated. As shown in **Figure 5(c),** increased temperature causes the free flow of electrons and holes, which then aids the transfer of heat from one point to another in solids, thus raising the thermal conductivity at elevated temperature and increasing the energy of electrons (Ahmed et al., 2017; Lahiri, 2005). The results are consistent in trend with those of many other similar DPs in literature (Aslam et al., 2021; Atsue & Oyewande, 2024; Haq et al., 2021; Noor et al., 2021). High Seebeck coefficient and electrical conductivity values with low electronic thermal conductivity values are anticipated from materials to boost the efficiency of a thermoelectric device. This suggests that the desired electronic thermal conductivity value to achieve the optimum efficiency can be obtained at a room temperature of 300 K. The peak value of the κ_e is $7.04\times10^{14}\ Wm^{-1}K^{-1}s^{-s}$ at 300 K in **Figure 5(a)** and is increased to $16.96\times10^{14}\ Wm^{-1}K^{-1}s^{-s}$ as the temperature is elevated to 800 K. Around the chemical potential values of -1.8 to 1.0 eV, the κ_e values at 300 K is zero. In **Figure 5(b)**, the peak value of the κ_e is $5.95\times10^{14}\ Wm^{-1}K^{-1}s^{-s}$ at 300 K which increased to $15.36\times10^{14}\ Wm^{-1}K^{-1}s^{-s}$ as the temperature is elevated to 800 K. The zero values of κ_e at 300 K are observed around the chemical potential values of -1.1 to 0.7 eV. The peaks of the thermal conductivity are also noticed to occur in the p-type region similar to the electrical conductivity of the materials.

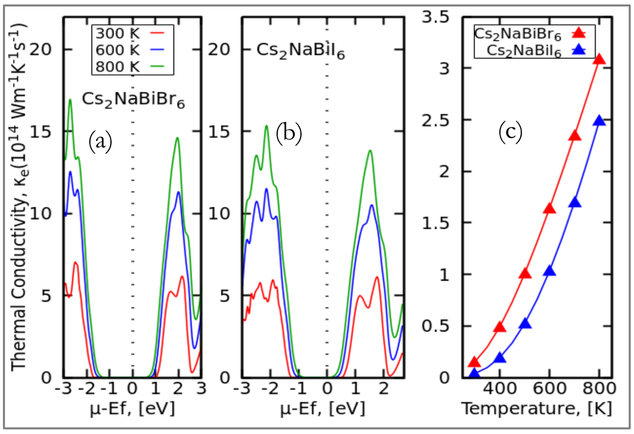

Figure 5: Chemical potential and temperature dependent electronic thermal conductivity curves for (a) $Cs_2NaBiBr_6$, (b) Cs_2NaBiI_6 DPs, and (c) electronic thermal conductivity as a function of temperature.

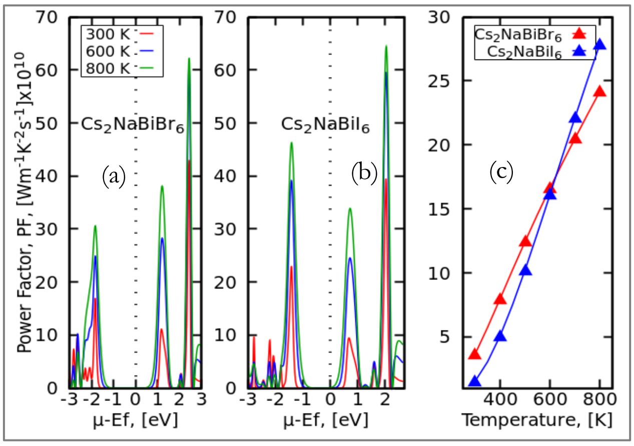

Figure 6: Chemical potential and temperature dependent electronic power factor curves for (a) $Cs_2NaBiBr_6$, (b) Cs_2NaBiI_6 DPs, and (c) power factor as a function of temperature.

Power factor (PF) is an essential thermoelectric property evaluated by the square of the Seebeck coefficient multiplied by the electrical conductivity ($i.e. PF = S^2\sigma$). This means that obtaining high PF entails reasonable values of the Seebeck coefficient and the electrical conductivity, which can boost the thermoelectric figure of merit (ZT). The electronic power factor obtained in this study is presented in Figure 6 for temperature values 300 K, 600 K, and 800 K, respectively. The curves are plotted as a function of the chemical potential ranging from -3.0 eV to 3.0 eV. The results show an increasing trend in the PF values as the temperature is elevated from 300 K to 800 K, as depicted in Figure 6(c). Several peaks are exhibited across the whole range of the chemical potential, but the maximum values appear within the positive region (n-type) of the chemical potential. For $Cs_2NaBiBr_6$ DP in Figure 6(a) at room temperature, the maximum PF is $43.024 \times 10^{10}\ Wm^{-1}K^{-2}s^{-1}$ while at an elevated temperature of 800 K, the PF value increased to a maximum of $62.270 \times 10^{10}\ Wm^{-1}K^{-2}s^{-1}$. At the chemical potential values of around -1.6 to $1.0\ eV$, zero PF values were observed at room temperature, and the region of zero PF values is narrowed at elevated temperature. In the case of Cs_2NaBiI_6 DP in Figure 6(b), the maximum PF at room temperature is $39.496 \times 10^{10}\ Wm^{-1}K^{-2}s^{-1}$ which increased to $64.412 \times 10^{10}\ Wm^{-1}K^{-2}s^{-1}$ at an elevated temperature of 800 K. Here, the zero PF at room temperature occurs around $-1.2\ eV$ to $0.4\ eV$ chemical potentials with a narrower region as the temperature increases.

In contrast to the maximum values of the Seebeck coefficient and electrical conductivity, the power factor at maximum values appeared to be independent of chemical potential as noticed from the plots. The power factor values have their peaks in the n-type region, whereas the Seebeck coefficient and electrical conductivity have their peaks in the p-type region of the materials. This, however, does not violet the proportionality of the power factor to the Seebeck coefficient and electrical conductivity. There is an inverse relationship between the Seebeck coefficient and electrical conductivity, with their peaks occurring at distinct chemical potential values. This suggests high electrical conductivity values can arise at lower Seebeck coefficient values and vice versa. This can change the position of the power factor peaks, as observed here and in other studies (Ahmed et al., 2017).

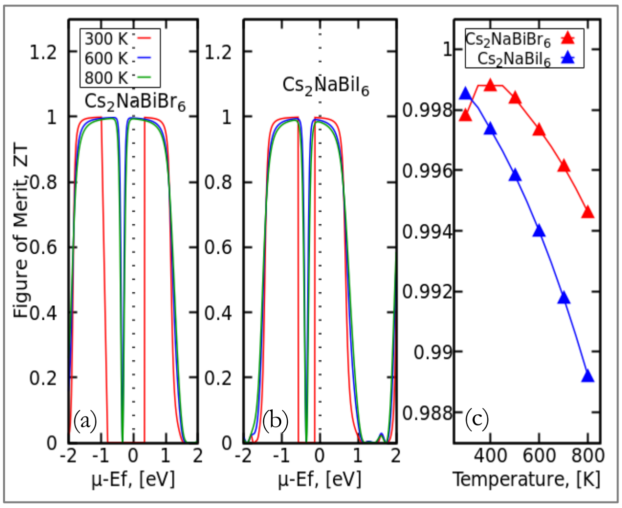

Figure 7: Chemical potential and temperature dependent thermoelectric figure of merit curves for (a) $Cs_2NaBiBr_6$, (b) Cs_2NaBiI_6 DPs, and (c) Figure of merit as a function of temperature.

For a thermoelectric device, its performance is measured by a non-dimension quantity called the thermoelectric figure of merit (ZT) given by $ZT = \frac{S^2\sigma}{\kappa}T$. Low thermal conductivity with high Seebeck coefficient and electrical conductivity is expected to boost the thermoelectric performance, as earlier buttressed. The chemical potential dependent ZT as computed at different temperatures of 300 K, 600 K, and 800 K are presented graphically in

Figure 7. The results of the ZT exhibit a slight decrease in values at temperature elevation from 300 K to 800 K for all DPs investigated. The temperature-dependent ZT is displayed in **Figure 7(c)** showing the the decrease with temperature. The ZT values at all temperatures are near unity suggesting the materials may be reasonable for thermoelectric applications. For $Cs_2NaBiBr_6$ DP in **Figure 7(a)**, the maximum ZT value at room temperature is 0.999, which decreases slightly to 0.995 at an elevated temperature of 800 K. For Cs_2NaBiI_6 DP in **Figure 7(b)**, a maximum value of 0.998 for ZT was observed at room temperature with a slight decrease to 0.985 at a temperature elevation of 800 K. Though the DP materials showed optimum performance at room temperature, the results suggest that thermoelectric device from these DP materials can be operated at high temperatures up to 800 K with reasonable efficiency.

Mechanical properties

The elastic constants are required to determine a crystal material's mechanical stability. For a cubic crystal, only three elastic constants are necessary, which are C_{11}, C_{12}, and C_{44}. This study used Thermo_pw code (Dal Corso, 2016) to compute the elastic constants. The conditions for mechanical stability of a cubic crystal according to Born criteria (Born, 1940) are given by $[C_{11} - C_{12} > 0,\ C_{44} > 0,\ C_{11} + 2C_{12} > 0, \text{and } C_{12} < B < C_{11}]$. Here, the material's bulk modulus is represented by B. **Table 1** presents the findings of the mechanical properties. According to the findings, the stability conditions established have been satisfied by the materials.

The average Voigt-Reuss-Hill (VRH) approximation is used to estimate these properties. The extent to which a crystal can resist fracture depends on the magnitude of its bulk modulus given by $B = \frac{C_{11} + 2C_{12}}{3}$, while its ability to withstand shear deformation is measured by the shear modulus given by $G = \frac{G_V + G_R}{2}$ according to the Voigt-Reuss-Hill (VRH) average approximation. The Voigt's shear modulus is determined from $G_V = \frac{(C_{11} - C_{12} + 3C_{44})}{5}$, while Reuss's shear modulus is given by $G_R = \frac{5(C_{11} - C_{12})C_{44}}{4C_{44} + 3(C_{11} - C_{12})}$. The results showed improved bulk and shear moduli as iodine is replaced by bromine in the perovskite compound. This may be attributed to the short ionic radius of bromine compared to iodine leading to stronger inter-atomic bonds. Conversely, the quantity of Young's modulus modulus, (E) given by $E = \frac{9BG}{3B + G}$ (Li et al., 2019), determines the strength of tensile stiffness in a solid material. The findings revealed the bromide DP to be stiffer than the iodide type.

A crystal material is anisotropic if the anisotropic factor (A) calculated from the relation $A = 2C_{44}/(C_{11} - C_{12})$ (Chung & Buessem, 1967) deviates from one (1) ($i.e. A < 1 \text{ or } A > 1$). The DP compounds examined in this study all had anisotropic values lower than one, proving that they are all naturally anisotropic.

Table 1: Elastic constants and other derived mechanical properties computed and presented here include the Elastic anisotropy (A), Bulk modulus (B), Young modulus (E), Shear modulus (G), Poisson's ratio (v), Pugh,s ratio (B/G), Vicker's hardness (H_v), Debye temperature (Θ_D), melting temperature (T_m), Kleinman's parameter (ζ), and Lame's coefficients (λ and μ).

	$Cs_2NaBiBr_6$	Cs_2NaBiI_6
C_{11} (GPa)	36.246	25.050
C_{12} (GPa)	5.745	2.912
C_{44} (GPa)	6.448	4.577
A	0.423	0.413
B (GPa)	15.912	10.291
E (GPa)	23.067	16.246
G (GPa)	9.176	6.577
v	0.258	0.235
B/G	1.734	1.565
ζ	0.310	0.267
λ (GPa)	9.774	8.896
μ (GPa)	9.168	6.577
H_v (GPa)	1.386	0.993
$\Theta_D (K)$	141.133	109.228
T_m (K)	782.151	648.603

Pugh's ratio, determined by B/G is a metric for determining a material's ductility or brittleness (Pugh, 1954). A material is ductile if its Pugh's ratio is greater than 1.75 and brittle otherwise (Luan et al., 2018). The results revealed that the DP compounds are brittle as their Pugh's ratio values are less than 1.75. The Poisson's ratio (v) defined by $v = \frac{3B - E}{6B}$ is a property of a material that confirms its ductility/brittleness similar to the Pugh's ratio. It also determines a material's bonding nature. The threshold of Poisson's ratio at which a material remains ductile is 0.26. Brittle materials have values of Poisson's ratio less than this threshold (Murtaza et al., 2014). The Poisson's ratio results for the DP compounds, therefore, supported Pugh's ratio findings, revealing the brittleness of the materials. The range of values of Poisson's ratio from 0.0 to 0.5 classifies materials according to different types of bonding. These are covalent, ionic, and metallic bonding, respectively. Covalent bond crystals have Poisson's ratio values around 0.1, whereas ionic bond crystals have values around 0.25. A material is classified as metallic bonded if Poisson's ratio value is around 0.33 (Murtaza et al., 2014). According to the findings in **Table 1**, the investigated DP compounds are most appropriately categorized as ionic bonded.

The Kleinman's parameter (ζ) given by $\zeta = \frac{C_{11}+8C_{12}}{7C_{11}+2C_{12}}$ is a measure of the bond strength of a crystal compound. It determines the ability of a bond to bend or to stretch (Osafile & Nenuwe, 2021). Bond stretching is observed when ζ values are approaching one while bond bending is observed for ζ values approaching zero. In the context of this investigation, bond bending is probably preferred. The compressive and shear stiffness of a crystal compound are measured by the Lame's constants (λ and μ). The first Lame's constant that measures the compressive stiffness is given by $\lambda = \frac{Ev}{(1+v)(1-2v)}$, while the second Lame's constant measuring the shear stiffness is defined by $\mu = \frac{E}{2(1+v)}$ (Osafile & Nenuwe, 2021). The findings revealed low compressive and shear stiffness for the DP compounds investigated. The findings, however, revealed that replacing iodine with bromine guarantees improved compressive and shear stiffness. Vickers hardness H_v is used to determine a material's capacity to withstand deformations like stretching or denting. Chen *et al* (X.-Q. Chen et al., 2011) asserts that, for brittle materials, the empirical formula $H_v = 0.151G$, could give the required Vickers hardness. The results demonstrate the poor Vickers hardness of the examined DP compounds, however, the Vickers hardness of the bromide DP is greater.

To determine the bonding lattice stability between the atoms, the Debye temperature (Θ_D) is estimated for both compounds using the relation (Al-Muhimeed et al., 2022; Li et al., 2019; Osafile & Nenuwe, 2021) $\Theta_D = \frac{h}{k}\left\{\frac{3n}{4\pi}\left(\frac{N_A\rho}{M}\right)\right\}^{\frac{1}{3}} V$. From the formula, h represents Plank's constant while the Boltzmann constant is represented by k. The Avogadro's constant is given by N_A, the density represented by ρ, a single cell weight is M, and the unit cell contains n number of atoms. The results suggest that the DP compounds possess reasonably high Debye temperature. The melting temperature (T_m) for a cubic compound is given by the empirical formula (Al-Muhimeed et al., 2022) $T_m = 412 + \{8.2 \times (C_{11} + C_{12}^{1.25})\}$. High melting and Debye temperatures for any compound material suggest the ionic nature of bonding for that material (Al-Muhimeed et al., 2022). To this extent, the findings of this study confirmed the ionic nature of the materials as predicted by Poisson's ratio. Our findings show the compound materials exhibit lower bulk modulus (B) and share modulus (G) than those of the similar perovskites by Haque *et al.* (2019).

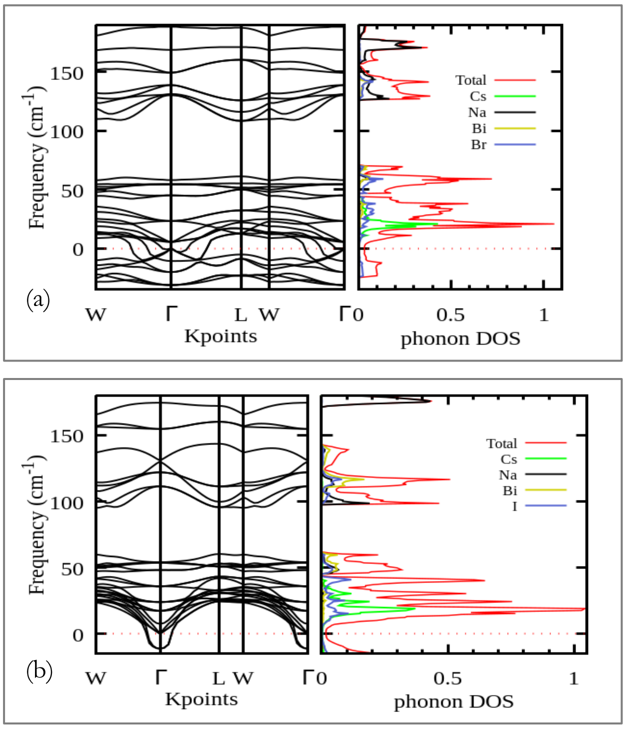

Figure 8: Phonon dispersion curves of the DPs (a) $Cs_2NaBiBr_6$, and (b) Cs_2NaBiI_6 with their corresponding phonon DOS.

Vibrational Properties

Electron-phonon interaction in a material can be understood from its vibrational properties (lattice dynamics). The lattice dynamics can also affect the material's thermal conductivity, which should be low for efficient thermoelectric performance. The anharmonic coupling between optical and acoustic phonons causes a strong acoustic phonon scattering (Tomczak, 2018), resulting in weak elastic characteristics and soft phonon modes that contribute to negative phonon frequencies in the phonon dispersion curves (Kagdada et al., 2018; Tomczak, 2018). This results in ultralow lattice thermal conductivity for a material as confirmed by numerous researchers (Acharya et al., 2016; Chang & Zhao, 2018; Chatterji et al., 2018; Luo et al., 2018; Roychowdhury et al., 2018) thus improving its thermoelectric figure of merit. However, due to computational costs and a lack of high memory computational resources, lattice thermal conductivity calculation was not taken into consideration in this study.

The vibrational properties were assessed by the computation of phonon frequency curves, to investigate the dynamical phonon stability of DP materials. The computation of the phonon dispersion curve takes into consideration the atomic resolved phonon density of states (DOS) to understand the role of each atom. As shown in **Figure 8**, points of high symmetry (W, Γ, L) in the vibrational Brillouin zone (BZ) were used in plotting the phonon dispersion curves. Observation of the phonon dispersion curves showed that at the Γ point, the phonon acoustic modes gradually tend to zero, satisfying the acoustic sum rule.

The structural stability based on the dynamics of phonons can be established depending on whether or not there exist phonon soft modes (imaginary phonon modes) within the curves of phonon frequency. According to the results in **Figure 8**, phonon soft modes exist in the phonon dispersion curves for all the DP compounds studied, suggesting structural instabilities. The analysis of the atomic resolved phonon DOS revealed that, these soft modes are primarily attributed to the halogen atoms (Br and I) in the compounds.

In the case of $Cs_2NaBiBr_6$ DP compound **in Figure 8 (a)**, the imaginary modes were observed across all points of high symmetry, suggesting both ferroelectric and anti-ferroelectric distortions. However, in the case of Cs_2NaBiI_6 DP compound **in Figure 8 (b)**, with the imaginary modes only present at the BZ center (Γ), ferroelectric distortion was possible. This is because the soft modes present at the BZ boundaries result in anti-ferroelectric distortion, whereas it results in ferroelectric distortion at the BZ center (Γ), and this is consistent with the results presented by (Jong et al., 2018; Jong et al., 2019).

CONCLUSION

This study investigated the transport properties of Cs_2NaBiX_6 DPs using the classical Boltzmann theory to understand their potential for applications in the thermoelectric field. The transport coefficients investigated include the Seebeck coefficient, electrical conductivity, thermal conductivity, the power factor, and the thermoelectric figure of merit. High Seebeck coefficient and electrical conductivity were obtained, as well as low thermal conductivity, which are the key factors for thermoelectric efficiency. As a result, the thermoelectric figure of merit near unity was obtained at room temperature and elevated temperatures up to 800 K, suggesting that thermoelectric devices from these DPs can be operated even at high temperatures. The study also evaluated the mechanical stability of the DPs by calculating the elastic constants of the material. The mechanical stability was evaluated based on the Born stability criteria for cubic crystals given by $C_{11} - C_{12} > 0$, $C_{44} > 0,\ C_{11} + 2C_{12} > 0$, and $C_{12} < B < C_{11}$. Therefore, these DPs satisfied all the Born stability criteria and are stable mechanically. The DPs were, however found to lack dynamical stability owing to the imaginary frequencies observed in the phonon dispersion curves. Therefore, the DPs under investigation have potential for deployment in thermoelectric applications subject to improving their dynamical stability. The materials could be investigated further for applications lasers and other optoelectronic devices

ACKNOWLEDGMENT

Access to TWAS1 High-Performance Computational resources from the East African Institute for Fundamental Research (EAIFR) in Rwanda is greatly acknowledged for the success of this work.

COMPETING INTERESTS DECLARATION

We have no known conflicts of interest to disclose.

REFERENCES

Acharya, S., Pandey, J., & Soni, A. (2016). Soft phonon modes driven reduced thermal conductivity in self-compensated Sn1.03Te with Mn doping. *Applied Physics Letters, 109*(13), 1–6. **[Crossref]**

Ahmed, R., Masuri, N. S., Ul Haq, B., Shaari, A., AlFaifi, S., Butt, F. K., … Tahir, S. A. (2017). Investigations of electronic and thermoelectric properties of half-Heusler alloys XMgN (X = Li, Na, K) by first-principles calculations. *Materials and Design, 136*, 196–203. **[Crossref]**

Aisida, S. O., & Oyewande, O. E. (2015). Move-biased Monte Carlo simulation method for amino acid gyration in protein native structure prediction. *African Review of Physics, 10*(1), 465–473.

Al-Muhimeed, T. I., Aljameel, A. I., Mera, A., Saad, S., Nazir, G., Albalawi, H., … Mahmood, Q. (2022). First principle study of optoelectronic and mechanical properties of lead-free double perovskites Cs2SeX6 (X = Cl, Br, I). *Journal of Taibah University for Science, 16*(1), 155–162. **[Crossref]**

Aslam, F., Sabir, B., & Hassan, M. (2021). Structural, electronic, optical, thermoelectric, and transport properties of indium-based double perovskite halides Cs2InAgX6 (X = Cl, Br, I) for energy applications. *Applied Physics A: Materials Science and Processing, 127*(2), 1–12. **[Crossref]**

Atsue, T., Ogunniranye, I. B., & Oyewande, O. E. (2021). Investigation of material properties of halide mixed lead-free double perovskite for optoelectronic applications using first-principles study. *Materials Science in Semiconductor Processing, 133*(10), 105963. **[Crossref]**

Atsue, T., & Oyewande, O. E. (2024). First-principles study of the structural, mechanical, dynamical, and transport properties of Cs2NaInX6 [X = Br, I] for thermoelectric applications. *Current Applied Physics, 57*(November 2023), 70–78. **[Crossref]**

Atsue, T., & Oyewande, O. E. (2024). Investigating the CsAuX3 [X = Cl, Br, I] perovskite materials properties responsible for photovoltaic applications: A first-principles study. *Computational Materials Science, 236*(February), 112881. **[Crossref]**

Bairwa, J. K., Kamlesh, P. K., Rani, U., Singh, R., Gupta, R., Kumari, S., … Verma, A. S. (2024). Highly efficient and stable Ra2LaNbO6 double perovskite for energy conversion device applications. *Materials Science for Energy Technologies, 7*(April 2023), 61–72. **[Crossref]**

Born, M. (1940). On the stability of crystal lattices. I. *Mathematical Proceedings of the Cambridge Philosophical Society, 36*(2), 160–172. **[Crossref]**

Broyden, C. G. (1970a). The convergence of a class of double-rank minimization algorithms: 2. The new algorithm. *IMA Journal of Applied Mathematics (Institute of Mathematics and Its Applications), 6*(3), 222–231. **[Crossref]**

Broyden, C. G. (1970b). The convergence of a class of double-rank minimization algorithms 1. General considerations. *IMA Journal of Applied Mathematics (Institute of Mathematics and Its Applications), 6*(1), 76–90. **[Crossref]**

Chang, C., & Zhao, L. D. (2018). Anharmonicity and low thermal conductivity in thermoelectrics. *Materials Today Physics, 4*, 50–57. **[Crossref]**

Chatterji, T., Wdowik, U. D., Jagło, G., Rols, S., & Wagner, F. R. (2018). Soft-phonon dynamics of the thermoelectric β-SnSe at high temperatures. *Physics Letters, Section A: General, Atomic and Solid State Physics, 382*(29), 1937–1941. **[Crossref]**

Chen, Q., Zhou, H., Hong, Z., Luo, S., Duan, H. S., Wang, H. H., … Yang, Y. (2014). Planar heterojunction perovskite solar cells via vapor-assisted solution process. *Journal of the American Chemical Society, 136*(2), 622–625. **[Crossref]**

Chen, X.-Q., Niu, H., Li, D., & Li, Y. (2011). Modeling hardness of polycrystalline materials and bulk metallic glasses. *Intermetallics, 19*(9), 1275–1281. **[Crossref]**

Chung, D. H., & Buessem, W. R. (1967). The elastic anisotropy of crystals. *Journal of Applied Physics, 38*(5), 2010–2012. **[Crossref]**

Dal Corso, A. (2016). Elastic constants of beryllium: A first-principles investigation. *Journal of Physics Condensed Matter, 28*(7). **[Crossref]**

Filip, M. R., & Giustino, F. (2016). Computational screening of homovalent lead substitution in organic-inorganic halide perovskites. *Journal of Physical Chemistry C, 120*(1), 166–173. **[Crossref]**

Filip, M. R., Hillman, S., Haghighirad, A. A., Snaith, H. J., & Giustino, F. (2016). Band gaps of the lead-free halide double perovskites Cs2BiAgCl6 and Cs2BiAgBr6 from theory and experiment. *Journal of Physical Chemistry Letters, 7*(13), 2579–2585. **[Crossref]**

Ghrib, T., Rached, A., Algrafy, E., Al-nauim, I. A., Albalawi, H., Ashiq, M. G. B., … Mahmood, Q. (2021). A new lead-free double perovskites K2Ti(Cl/Br)6; A promising material for optoelectronic and transport properties; Probed by DFT. *Materials Chemistry and Physics, 264*(September 2020), 124435. **[Crossref]**

Giannozzi, P., Andreussi, O., Brumme, T., Bunau, O., Buongiorno Nardelli, M., Calandra, M., … Baroni, S. (2017). Advanced capabilities for materials modelling with Quantum ESPRESSO. *Journal of Physics Condensed Matter, 29*(46), 465901. **[Crossref]**

Giannozzi, P., Baroni, S., Bonini, N., Calandra, M., Car, R., Cavazzoni, C., … Wentzcovitch, R. M. (2009). QUANTUM ESPRESSO: A modular and open-source software project for quantum simulations of materials. *Journal of Physics: Condensed Matter, 21*(39), 395502. **[Crossref]**

Hamann, D. R., Schlüter, M., & Chiang, C. (1979). Norm-conserving pseudopotentials. *Physical Review Letters, 43*(20), 1494–1497. **[Crossref]**

Hao, F., Stoumpos, C. C., Chang, R. P. H., & Kanatzidis, M. G. (2014). Anomalous band gap behavior in mixed Sn and Pb perovskites enables broadening of absorption spectrum in solar cells. *Journal of the American Chemical Society, 136*(22), 8094–8099. **[Crossref]**

Haq, A. U., Mustafa, G. M., Amin, M., Ramay, S. M., & Mahmood, A. (2021). Ab-initio study of opto-electronic and thermoelectric properties of direct bandgap double perovskites Rb2XGaBr6 (X = Na, K). *International Journal of Energy Research, 45*(6), 9241–9251. **[Crossref]**

Haque, E., & Hossain, M. A. (2019). Electronic, phonon transport, and thermoelectric properties of Cs2InAgCl6 from first-principles study. *Computational Condensed Matter, 19*, e00374. **[Crossref]**

Johnson, O. O., Olutuase, P. E., & Oyewande, O. E. (2019). First principles calculations of the optoelectronic properties of magnesium substitutes in lead-based ABX3 compounds. *Journal of Physics: Conference Series, 1299*(1), 012129. **[Crossref]**

Jong, U. G., Yu, C. J., Kye, Y. H., Kim, Y. S., Kim, C. H., & Ri, S. G. (2018). A first-principles study on the chemical stability of inorganic perovskite solid solutions Cs1-xRbxPbI3 at finite temperature and pressure. *Journal of Materials Chemistry A, 6*(37), 17994–18002. **[Crossref]**

Jong, U., Yu, C., Kye, Y., Choe, S., Kim, J., & Choe, Y. (2019). Anharmonic phonons and phase transitions in the vacancy-ordered double perovskite Cs2SnI6 from first-principles predictions. *Physical Review B, 99*(18), 1–8. **[Crossref]**

Joshi, T. K., Pravesh, Sharma, G., & Verma, A. S. (2020). Investigation of structural, electronic, optical, and thermoelectric properties of ethylammonium tin iodide (CH3CH2NH3SnI3): An appropriate hybrid material for photovoltaic application. *Materials Science in Semiconductor Processing, 115*(April), 105111. **[Crossref]**

Kagdada, H. L., Jha, P. K., Śpiewak, P., & Kurzydłowski, K. J. (2018). Structural stability, dynamical stability, thermoelectric properties, and elastic properties of GeTe at high pressure. *Physical Review B, 97*(13), 1–10. **[Crossref]**

Kattan, N. A., Mahmood, Q., Nazir, G., Rehman, A., Sfina, N., Al-anazy, M. M., … Amin, M. A. (2023). Modifying electronic bandgap by halide ions substitution to investigate double perovskites Rb2AgInX6 (X = Cl, Br, I) for solar cells applications and thermoelectric characteristics. *Materials Today Communications, 34*(December 2022), 105166. **[Crossref]**

Kim, H. S., Lee, C. R., Im, J. H., Lee, K. B., Moehl, T., Marchioro, A., … Park, N. G. (2012). Lead iodide perovskite sensitized all-solid-state submicron thin film mesoscopic solar cell with efficiency exceeding 9%. *Scientific Reports, 2*, 1–7. **[Crossref]**

Kokalj, A. (1999). XCrySDen—A new program for displaying crystalline structures and electron densities. *Journal of Molecular Graphics and Modelling, 17*(3–4), 176–179. **[Crossref]**

Kolebaje, O., Popoola, O., Khan, M. A., & Oyewande, O. (2020). An epidemiological approach to insurgent population modeling with the Atangana-Baleanu fractional derivative. *Chaos, Solitons & Fractals, 139*(109970), 109970. **[Crossref]**

Krishnamoorthy, T., Ding, H., Yan, C., Leong, W. L., Baikie, T., Zhang, Z., … Mhaisalkar, S. G. (2015). Lead-free germanium iodide perovskite materials for photovoltaic applications. *Journal of Materials Chemistry A, 3*(47), 23829–23832. **[Crossref]**

Lahiri, A. K. (2005). Transport phenomena and metals properties. In *Fundamentals of metallurgy* (pp. 178–236). **[Crossref]**

Leijtens, T., Prasanna, R., Gold-Parker, A., Toney, M. F., & McGehee, M. D. (2017). Mechanism of tin oxidation and stabilization by lead substitution in tin halide perovskites. *ACS Energy Letters, 2*(9), 2159–2165. **[Crossref]**

Li, H., Zhang, X., Liu, Q., Liu, Y., Liu, H., Wang, X., … Lei, G. (2019). First-principles calculations of mechanical and thermodynamic properties of tungsten-based alloy. *Nanotechnology Reviews, 8*(1), 258–265. **[Crossref]**

Luan, X., Qin, H., Liu, F., Dai, Z., Yi, Y., & Li, Q. (2018). The mechanical properties and elastic anisotropies of cubic Ni3Al from first principles calculations. *Crystals, 8*(8), 307. **[Crossref]**

Luo, Z. Z., Hao, S., Zhang, X., Hua, X., Cai, S., Tan, G., … Kanatzidis, M. G. (2018). Soft phonon modes from off-center Ge atoms lead to ultralow thermal conductivity and superior thermoelectric performance in n-type PbSe-GeSe. *Energy and Environmental Science, 11*(11), 3220–3230. **[Crossref]**

Lyu, M., Yun, J., Chen, P., Hao, M., & Wang, L. (2017). Addressing toxicity of lead: Progress and applications of low-toxic metal halide perovskites and their derivatives. *Advanced Energy Materials, 7*(15), 1602512. **[Crossref]**

Mahmood, Q., Yaseen, M., Ul Haq, B., Laref, A., & Nazir, A. (2019). The study of mechanical and thermoelectric behavior of MgXO3 (X = Si, Ge, Sn) for energy applications by DFT. *Chemical Physics, 524*(May), 106–112. **[Crossref]**

McClure, E. T., Ball, M. R., Windl, W., & Woodward, P. M. (2016). Cs2AgBiX6 (X = Br, Cl): New visible light absorbing, lead-free halide perovskite semiconductors. *Chemistry of Materials, 28*(5), 1348–1354. **[Crossref]**

Mera, A., Nazir, G., Mahmood, Q., Kattan, N. A., Alshahrani, T., Rehman, A., … Elhosiny Ali, H. (2023). The bandgap engineering of double perovskites Cs2CuSbX6 (X = Cl, Br, I) for solar cell and thermoelectric applications. *Inorganic Chemistry Communications, 148*(December 2022), 110303. **[Crossref]**

Moniruddin, M., Ilyassov, B., Zhao, X., Smith, E., Serikov, T., Ibrayev, N., … Nuraje, N. (2018). Recent progress on perovskite materials in photovoltaic and water splitting applications. *Materials Today Energy, 7*, 246–259. **[Crossref]**

Murnaghan, F. D. (1924). The volume changes of five gases under high pressures. *Journal of the Franklin Institute, 197*(1), 98. **[Crossref]**

Murtaza, G., Gupta, S. K., Seddik, T., Khenata, R., Alahmed, Z. A., Ahmed, R., … Bin Omran, S. (2014). Structural, electronic, optical, and thermodynamic properties of cubic REGa3 (RE = Sc or Lu) compounds: Ab initio study. *Journal of Alloys and Compounds, 597*, 36–44. **[Crossref]**

Noor, N. A., Iqbal, M. W., Zelai, T., Mahmood, A., Shaikh, H. M., Ramay, S. M., & Al-Masry, W. (2021). Analysis of direct band gap A2ScInI6 (A = Rb, Cs) double perovskite halides using DFT approach for renewable energy devices. *Journal of Materials Research and Technology, 13*, 2491–2500. **[Crossref]**

Ogunniranye, I. B., Atsue, T., & Oyewande, O. E. (2021). Structural and optoelectronic behavior of the copper-doped Cs2AgInCl6 double perovskite: A density functional theory investigation. *Physical Review B, 103*(2), 024102. **[Crossref]**

Osafile, O. E., & Nenuwe, O. N. (2021). Lattice dynamics and thermodynamic responses of XNbSn half-Heusler semiconductors: A first-principles approach. *Journal of the Nigerian Society of Physical Sciences, 3*(2), 121–130. **[Crossref]**

Oyewande, O., & Adeoti, B. (2014). Theory of off-normal incidence ion sputtering of surfaces of type A_xB_{1-x} and a conformal map method for stochastic continuum models. *The African Review of Physics, 9*(0024), 177–183.

Oyewande, O. E. (2012). A unified spatio-temporal framework of the Cuerno-Barabasi stochastic continuum model of surface sputtering. *Communications in Theoretical Physics, 58*(1), 165–170. **[Crossref]**

Oyewande, O. E. (2013). Phase boundaries of nano-dots and nano-ripples over a range of collision cascades. *The African Review of Physics, 8*(44), 313–316. **[Crossref]**

Pack, J. D., & Monkhorst, H. J. (1977). Summary for policymakers. In *Climate change 2013 - The physical science basis* (Vol. 53, pp. 1–30). **[Crossref]**

Perdew, J. P., Ruzsinszky, A., Csonka, G. I., Vydrov, O. A., Scuseria, G. E., Constantin, L. A., … Burke, K. (2008). Restoring the density-gradient expansion for exchange in solids and surfaces. *Physical Review Letters, 100*(13), 1–4. **[Crossref]**

Pitaro, M., Tekelenburg, E. K., Shao, S., & Loi, M. A. (2022). Tin halide perovskites: From fundamental properties to solar cells. *Advanced Materials, 34*(1). **[Crossref]**

Pugh, S. F. (1954). Relations between the elastic moduli and the plastic properties of polycrystalline pure metals. *The London, Edinburgh, and Dublin Philosophical Magazine and Journal of Science, 45*(367), 823–843. **[Crossref]**

Roknuzzaman, M., Zhang, C., Ostrikov, K. (Ken), Du, A., Wang, H., Wang, L., & Tesfamichael, T. (2019). Electronic and optical properties of lead-free hybrid double perovskites for photovoltaic and optoelectronic applications. *Scientific Reports, 9*(1), 1–7. **[Crossref]**

Roychowdhury, S., Jana, M. K., Pan, J., Guin, S. N., Sanyal, D., Waghmare, U. V., & Biswas, K. (2018). Soft phonon modes leading to ultralow thermal conductivity and high thermoelectric performance in AgCuTe. *Angewandte Chemie - International Edition, 57*(15), 4043–4047. **[Crossref]**

Shi, H., & Du, M.-H. (2015). Discrete electronic bands in semiconductors and insulators: Potential high-light-yield scintillators. *Physical Review Applied, 3*(5), 054005. **[Crossref]**

Sholl, D. S., & Steckel, J. A. (2009). *Density functional theory: A practical introduction*. Wiley. **[Crossref]**

Slavney, A. H., Hu, T., Lindenberg, A. M., & Karunadasa, H. I. (2016). A bismuth-halide double perovskite with long carrier recombination lifetime for photovoltaic applications. *Journal of the American Chemical Society, 138*(7), 2138–2141. **[Crossref]**

Slavney, A. H., Smaha, R. W., Smith, I. C., Jaffe, A., Umeyama, D., & Karunadasa, H. I. (2017). Chemical approaches to addressing the instability and toxicity of lead-halide perovskite absorbers. *Inorganic Chemistry, 56*, 46–55. **[Crossref]**

Tomczak, J. M. (2018). Thermoelectricity in correlated narrow-gap semiconductors. *Journal of Physics Condensed Matter, 30*(18). **[Crossref]**

Volonakis, G., Filip, M. R., Haghighirad, A. A., Sakai, N., Wenger, B., Snaith, H. J., & Giustino, F. (2016). Lead-free halide double perovskites via heterovalent substitution of noble metals. *Journal of Physical Chemistry Letters, 7*(7), 1254–1259. **[Crossref]**

Yang, Z., Rajagopal, A., Chueh, C. C., Jo, S. B., Liu, B., Zhao, T., & Jen, A. K. Y. (2016). Stable low-bandgap Pb-Sn binary perovskites for tandem solar cells. *Advanced Materials, 28*(40), 8990–8997. **[Crossref]**

Yewande, E. O., Hartmann, A. K., & Kree, R. (2005). Propagation of ripples in Monte Carlo models of sputter-induced surface morphology. *Physical Review B, 71*(19), 195405. **[Crossref]**

Yewande, E. O., Kree, R., & Hartmann, A. K. (2006). Morphological regions and oblique-incidence dot formation in a model of surface sputtering. *Physical Review B - Condensed Matter and Materials Physics, 73*(11), 1–8. **[Crossref]**

Yewande, E. O., Kree, R., & Hartmann, A. K. (2007). Numerical analysis of quantum dots on off-normal incidence ion sputtered surfaces. *Physical Review B - Condensed Matter and Materials Physics, 75*(15), 14–16. **[Crossref]**

Yewande, E. O., Neal, M. P., & Low, R. (2009). The Hausdorff chirality measure and a proposed Hausdorff structure measure. *Molecular Physics, 107*(3), 281–291. **[Crossref]**

Yewande, O. E., Moreno, Y., Kun, F., Hidalgo, R. C., & Herrmann, H. J. (2003). Time evolution of damage under variable ranges of load transfer. *Physical Review E, 68*(2), 026116. **[Crossref]**

Zhao, S., Yamamoto, K., Iikubo, S., Hayase, S., & Ma, T. (2018). First-principles study of electronic and optical properties of lead-free double perovskites Cs2NaBX6 (B = Sb, Bi; X = Cl, Br, I). *Journal of Physics and Chemistry of Solids, 117*, 117–121. **[Crossref]**